ADVANCED ENERGY MATERIALS
www.advenergymat.de

A Solvothermal Synthetic Environmental Design for High-Performance SnSe-Based Thermoelectric Materials

*Xiao-Lei Shi, Wei-Di Liu, Meng Li, Qiang Sun, Sheng-Duo Xu, Du Du, Jin Zou, and Zhi-Gang Chen**

SnSe is challenging to use in thermoelectric devices due to difficulties in simultaneously optimizing its thermoelectric and mechanical properties. Here, the authors show a unique solvothermal synthetic environmental design to fabricate super-large and micro/nanoporous $Sn_{0.965}Se$ microplates by using $CrCl_3$. Cl^- ions to trigger Sn-vacancy formation and optimize the hole concentration to ≈3×10^{19} cm^{-3}, while the as-formed $Cr(OH)_3$ colloidal precipitations act as "templates" to achieve micro/nanoporous features, leading to low lattice thermal conductivity of ≈0.2 W m^{-1} K^{-1} in the as-sintered polycrystal, contributing to a high *ZT* of ≈2.4 at 823 K and an average *ZT* of ≈1.1. Of particular note, the polycrystal exhibits high hardness (≈2.26 GPa) and compression strength (≈109 MPa), strengthened by grain refinement and vacancy-induced lattice distortions; while a single-leg device provides a stable output power (>100 mW) and conversion efficiency of ≈10% by a temperature difference of 425 K, indicating great potential for applying to practical thermoelectric devices.

1. Introduction

With the rapid development of human society, fossil fuels are increasingly depleted, and the resulting environmental pollution is becoming increasingly serious. To relieve the significant stress from energy depletion in the future, sustainable power generation and refrigeration solutions are urgently needed. Thermoelectric materials and devices can realize direct conversions between heat and electricity, therefore have exhibited the considerable potential to tackle the above issues.[1] To boost the thermoelectric conversion efficiency of the thermoelectric devices, the n-type and p-type materials as core components in the devices must possess high dimensionless figure-of-merit *ZT* values, which can be determined by $ZT = (S^2\sigma/\kappa) \cdot T$.[2] Here $S^2\sigma$ is the power factor that is composed of Seebeck coefficient S and electrical conductivity σ, κ is the thermal conductivity that is composed of electronic thermal conductivity κ_e and lattice thermal conductivity κ_l ($\kappa = \kappa_e + \kappa_l$), and T is the absolute temperature,[3] respectively. To date, optimizing the $S^2\sigma$ by tuning the carrier concentration n (n_p for p-type materials with holes as major carriers and n_e for n-type materials with electrons as major carriers), and reducing the κ_l by rational structural engineering, are two effective strategies for achieving high *ZT*s in current thermoelectric materials;[4] while exploring new thermoelectric materials with intrinsic high S and low κ_l is also of significance.[5]

Benefiting from the developed thermoelectric science and technology, many thermoelectric materials have been reported with high *ZT*s of >2, such as GeTe,[6] Cu_2Se,[7] PbTe,[8] and SnSe.[9] Among these state-of-the-art materials, SnSe is known as a promising candidate with full potential for assembling thermoelectric devices because of its high-performance, low-toxic, and cost-effective features, thus has attracted intensive attention in recent years.[9] SnSe possesses a suitable bandgap of ≈0.9 eV (low-temperature α-SnSe, Figure S1, Supporting Information),[9] which is a typical p-type semiconductor with an intrinsic high S of >300 μV K^{-1}. Meanwhile, SnSe possesses a typical layered crystal structure, in which Sn-Se layers are stacked layer-by-layer along its out-of-plane direction with Van der Waals forces between the layers (Figure S2, Supporting Information), leading to much higher σ and $S^2\sigma$ along its in-plane direction.[9] Furthermore, SnSe possesses an intrinsic low κ_l derived from its unique zig-zag bonding between Sn and Se,[9] indicating significant potential in realizing high *ZT*. It was reported that p-type SnSe crystal showed a high *ZT* of ≈2.6 at 923 K along its *b*-axis,[10] while n-type Br-doped SnSe

X.-L. Shi, Z.-G. Chen
School of Chemistry and Physics
Queensland University of Technology
Brisbane, Queensland 4000, Australia
E-mail: zhigang.chen@qut.edu.au
W.-D. Liu
Australian Institute for Bioengineering and Nanotechnology
The University of Queensland
Brisbane, Queensland 4072, Australia
M. Li, S.-D. Xu, D. Du, J. Zou
School of Mechanical and Mining Engineering
The University of Queensland
Brisbane, Queensland 4072, Australia
Q. Sun, J. Zou
Centre for Microscopy and Microanalysis
The University of Queensland
Brisbane, Queensland 4072, Australia
The ORCID identification number(s) for the author(s) of this article can be found under https://doi.org/10.1002/aenm.202200670.

DOI: 10.1002/aenm.202200670

crystal exhibited a high ZT of ≈2.8 at 773 K along its a-axis.[11] However, because of their critical growth techniques, prospective high cost, and poor mechanical properties,[9] SnSe crystals are undesirable for assembling practical devices. Consequently, polycrystalline SnSe has become a potential alternative.[9] Till now, rational doping with other elements or alloying with other compounds have been commonly used to tune the n of polycrystalline SnSe and in turn optimize its $S^2\sigma$ (Figure S3, Supporting Information), while micro/nanostructure manipulations were employed to suppress its κ_l,[9] leading to improved ZTs. Texturing was also used to further improve the electrical transport of polycrystalline SnSe.[12] Benefiting from the synergy effect of Na-doping and oxide-removing, the ZT of p-type polycrystalline SnSe has been reported to reach 3.1 at 783 K,[13] which is even higher than that of the single crystals.[9] However, it was reported that Na-doping may severely damage the mechanical performance of SnSe, and the reported ultralow κ_l of only 0.07 W m^{-1} K^{-1} is difficult to understand.[13] Considering that a high-performing device requires both high average ZT (ZT_{ave}) within the entire temperature range[14] and high mechanical properties to resist internal or external forces during working,[4] developing mechanical-robust polycrystalline SnSe with high ZT_{ave} is still urgent.

To avoid damaging the mechanical properties of p-type polycrystalline SnSe, developing pure polycrystalline $Sn_{1-x}Se$ with rationally tuned Sn vacancy (V_{Sn}) concentration is a promising strategy, which can be described as "vacancy engineering". It was reported that V_{Sn} can strengthen the mechanical performance of polycrystalline $Sn_{1-x}Se$ by point-defect-induced reinforcement,[15] while rationally tuning the V_{Sn} concentration can simultaneously tune the n_p since introducing extra V_{Sn} can lower the Fermi level down into the valence bands and in turn generate hole carriers, confirmed by first-principles density functional theory (DFT) calculations (Figure S4, Supporting Information).[16,17] We analyze the relationship between the reported n_p and ZT values for pure polycrystalline $Sn_{1-x}Se$ by a classic single parabolic band (SPB) model[15,18–22] that is based on the condition of acoustic phonon scattering, and the results indicate that a high ZT of >2 requires both a well-tuned n_p of ≈3×10^{19} cm^{-3} and a low κ_l of <0.2 W m^{-1} K^{-1} at 823 K (**Figure 1**a). To achieve this goal, it is needed to combine the vacancy engineering with micro/nanostructuring to simultaneously achieve high $S^2\sigma$ and low κ_l, which is always tricky for conventional melting or mechanical alloying since these fabrication techniques are difficult to form V_{Sn} with a satisfied concentration and maintain a strong anisotropy in the polycrystalline $Sn_{1-x}Se$.

Aqueous-solution-based solvothermal synthesis is a route to fabricate super-large $Sn_{1-x}Se$ microplates with average dimensions of >100 μm.[15] By sintering these microplates into polycrystals, the as-achieved p-type $Sn_{1-x}Se$ can exhibit single-crystal-like anisotropy with high electrical transport performance along the direction perpendicular to the sintering pressure. The main chemical reactions during the solvothermal synthesis can be expressed as:[15]

$$SnCl_2 \cdot 2H_2O \xrightarrow{C_2H_6O_2} Sn^{2+} + 2Cl^- + 2H_2O \quad (1)$$

$$Na_2SeO_3 \xrightarrow{C_2H_6O_2} 2Na^+ + SeO_3^{2-} \quad (2)$$

$$SeO_3^{2-} + C_2H_6O_2 \rightarrow Se + C_2H_2O_2 + H_2O + 2OH^- \quad (3)$$

$$3Se + 6OH^- \rightarrow 2Se^{2-} + SeO_3^{2-} + 3H_2O \quad (4)$$

$$(1-x)Sn^{2+} + Se^{2-} \xrightarrow{Na^+} Sn_{1-x}Se \quad (5)$$

where $C_2H_6O_2$ acts as the solvent to dissolve $SnCl_2 \cdot 2H_2O$ as Sn sources (Equation 1) and Na_2SeO_3 as Se sources (Equation 2). $C_2H_6O_2$ also acts as the reducing agent to generate Se (Equation 3), and NaOH acts as the reducing agent to reduce Se into Se^{2-} (Equation 4), benefiting the formation of $Sn_{1-x}Se$ (Equation 5).[23–25] Based on the above chemical reactions, by tuning the NaOH concentration during the synthesis, rationally tuned V_{Sn} with a concentration of ≈2.5% can lead to a high n_p of ≈2.3×10^{19} cm^{-3} and in turn a high ZT of ≈1.5 at 823 K and a high ZT_{ave} of ≈0.8.[15] The as-achieved V_{Sn} can simultaneously improve the compression strength of polycrystalline $Sn_{1-x}Se$ from 52.1 MPa to 77.0 MPa.[15] However, the as-achieved n_p still needs further improvement (up to ≈3×10^{19} cm^{-3}) to optimize the ZT, and the as-achieved ZT of ≈1.5 is not competitive compared with reported ZTs of >2 in single crystals[10] and many other thermoelectric materials,[4] which is mainly resulted from its κ_l of >0.3 W m^{-1} K^{-1}. Furthermore, a higher ZT_{ave} of >1.0 should be further realized to be valuable for applying to practical devices.

In this work, we employ $CrCl_3$ during the solvothermal synthesis to simultaneously tune the n_p and suppress the κ_l of the as-fabricated $Sn_{1-x}Se$. In detail, we employ y% $CrCl_3$ as a multi-functional precursor during the solvothermal synthesis (Figure 1b), and y% is defined as the ratio of $CrCl_3$ to $SnCl_2 \cdot 2H_2O$ used for the synthesis. By dissolving $CrCl_3$ into the solution, there are chemical reactions:

$$CrCl_3 \xrightarrow{C_2H_6O_2} Cr^{3+} + 3Cl^- \quad (6)$$

$$Cr^{3+} + 3OH^- \xrightarrow{C_2H_6O_2} Cr(OH)_3 \quad (7)$$

Because dissolving $CrCl_3$ can release extra Cl^- in the solution (Equation 6), based on the common ion effect,[26] these extra Cl^- will inhibit the reaction of Equation 1, leading to a less-Sn condition in the as-synthesized $Sn_{1-x}Se$ microplates. We carefully studied the real compositions of polycrystalline $Sn_{1-x}Se$ sintered from these microplates by electron probe micro-analyser (EPMA), and the results indicated that with increasing the amount of $CrCl_3$ up to $y = 10$, the V_{Sn} concentration can be further increased from ≈1.9% to ≈3.5% (Figure 1c & Table S1–S2, Supporting Information), leading to a well-tuned n_p from ≈1.5×10^{19} cm^{-3} to ≈3.0×10^{19} cm^{-3}, which is the optimized value for achieving a peak $S^2\sigma$ of ≈8.35 μW cm^{-1} K^{-2} at 823 K. At the same time, during the synthesis, Cr^{3+} react with OH^- to form $Cr(OH)_3$ colloidal precipitations, confirmed by X-ray diffraction (XRD) patterns (Figure S5, Supporting Information) and scanning electronic microscopy (SEM) image (Figure S6, Supporting Information). During the crystal-growth process in the solution, these colloidal precipitations can realize unique micro/nanoporous structures of the as-synthesized $Sn_{1-x}Se$ microplates without reducing their dimensions (Figure S7, Supporting Information), acting as unique "templates". After the synthesis, all precipitations attached to the as-synthesized microplates can be removed by washing the

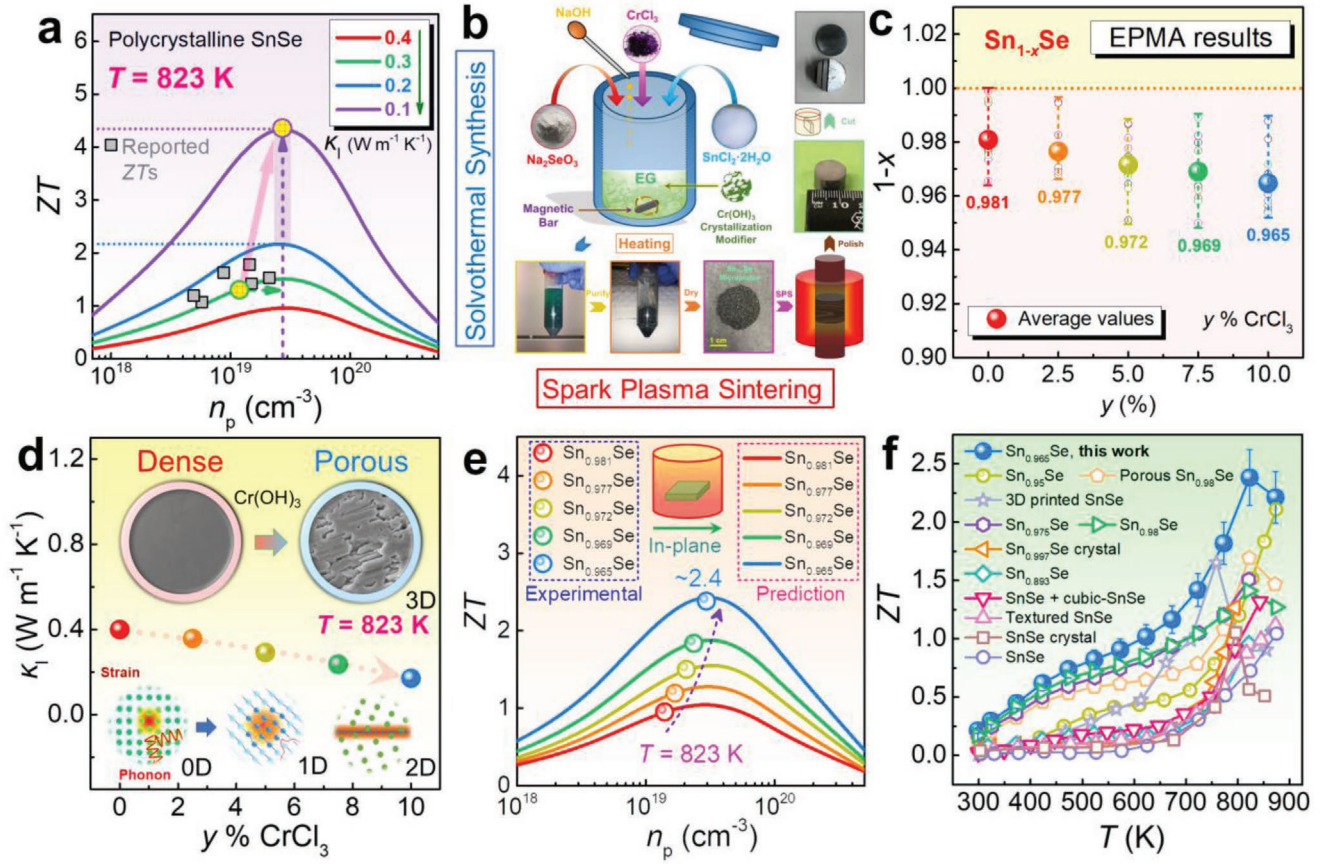

Figure 1. Fabrications, compositions, and thermoelectric performance of polycrystalline $Sn_{1-x}Se$. a) Figure-of-merit *ZT* as functions of hole carrier concentration n_p and lattice thermal conductivity κ_l for p-type polycrystalline SnSe at 823 K, calculated by a single parabolic band (SPB) model. Reported *ZT* values are provided for comparison.[15,18–22] b) Schematic diagram of fabricating polycrystalline $Sn_{1-x}Se$ by a combination of solvothermal synthesis and sparkle plasma sintering (SPS) technique. c) Real compositions of polycrystalline $Sn_{1-x}Se$ fabricated by using *y* % $CrCl_3$ during the solvothermal synthesis, evaluated by electron probe microanalysis (EPMA). Here *y* = 0, 2.5, 5, 7.5, and 10, respectively. d) κ_l of polycrystalline $Sn_{1-x}Se$ as a function of *y* % $CrCl_3$. The insets illustrate multi-dimensional crystal imperfections found in the matrix of polycrystalline $Sn_{1-x}Se$, including zero-dimensional (0D) point defects, one-dimensional (1D) edge dislocations, two-dimensional (2D) grain boundaries, and three-dimensional (3D) pores. e) n_p-dependent *ZT* for polycrystalline $Sn_{1-x}Se$ at 823 K, calculated by the SPB model. The as-achieved experimental *ZT* values are included for comparison. f) Temperature *T*-dependent *ZT* of polycrystalline $Sn_{0.965}Se$ by using 10% $CrCl_3$ during the solvothermal synthesis. Reported *T*-dependent *ZT* values are included for comparison.[15,17–22,27–30]

products with H_2O and ethanol. By sintering these micro/nanoporous microplates into polycrystals through a fast sparkle plasma sintering technique, we successfully obtained polycrystalline $Sn_{1-x}Se$ with dense grain boundaries and three-dimensional (3D) pores as defects while keeping a strong anisotropy (Figure S8, Supporting Information). Such a unique structure combined with other lattice imperfections such as zero-dimensional (0D) point defects and one-dimensional (1D) dislocations caused by introducing high-concentration V_{Sn} can successfully suppress the κ_l from ≈0.4 W m^{-1} K^{-1} to ≈0.2 W m^{-1} K^{-1} at 823 K (Figure 1d). As a result, a competitively high *ZT* of ≈2.4 can be achieved in polycrystalline $Sn_{0.965}Se$ at 823 K along the direction perpendicular to the sintering pressure, which has reached the peak value confirmed by the SPB model (Figure 1e). In addition to the high peak *ZT* at 823 K, a competitive ZT_{ave} of ≈1.1 can be simultaneously realized (Figure S9, Supporting Information), which is valuable for applying to practical thermoelectric devices. We also compare the *T*-dependent *ZT* between our polycrystalline $Sn_{0.965}Se$ and reported pure $Sn_{1-x}Se$[15,17–22,27–30] from room temperature to 873 K (Figure 1f), and the results indicate that the *ZT* of our $Sn_{0.965}Se$ is around 1.6 at 750 K, and the *ZT* is >1 within a wide temperature range of >600 K, unveiling the potential for applying to practical applications.

2. Results and Discussion

In addition to the optimized n_p of ≈3.0 × 10^{19} cm^{-3} and suppressed κ_l of ≈0.2 W m^{-1} K^{-1} that leads to the high peak *ZT* at 823 K, the strong anisotropy in the as-sintered polycrystal also plays a significant role in determining the high electrical transport performance. In this work, we found that there is an optimized concentration of $CrCl_3$ during the solvothermal synthesis, which is equal to using 10% $CrCl_3$ as precursors (*y* = 10). When the $CrCl_3$ concentration is <10%, the n_p is <3.0 × 10^{19} cm^{-3} due to the insufficient V_{Sn} concentration of <3.5%, and the pores in the microplates or as-sintered polycrystals are not dense due to the insufficient $Cr(OH)_3$ formed during

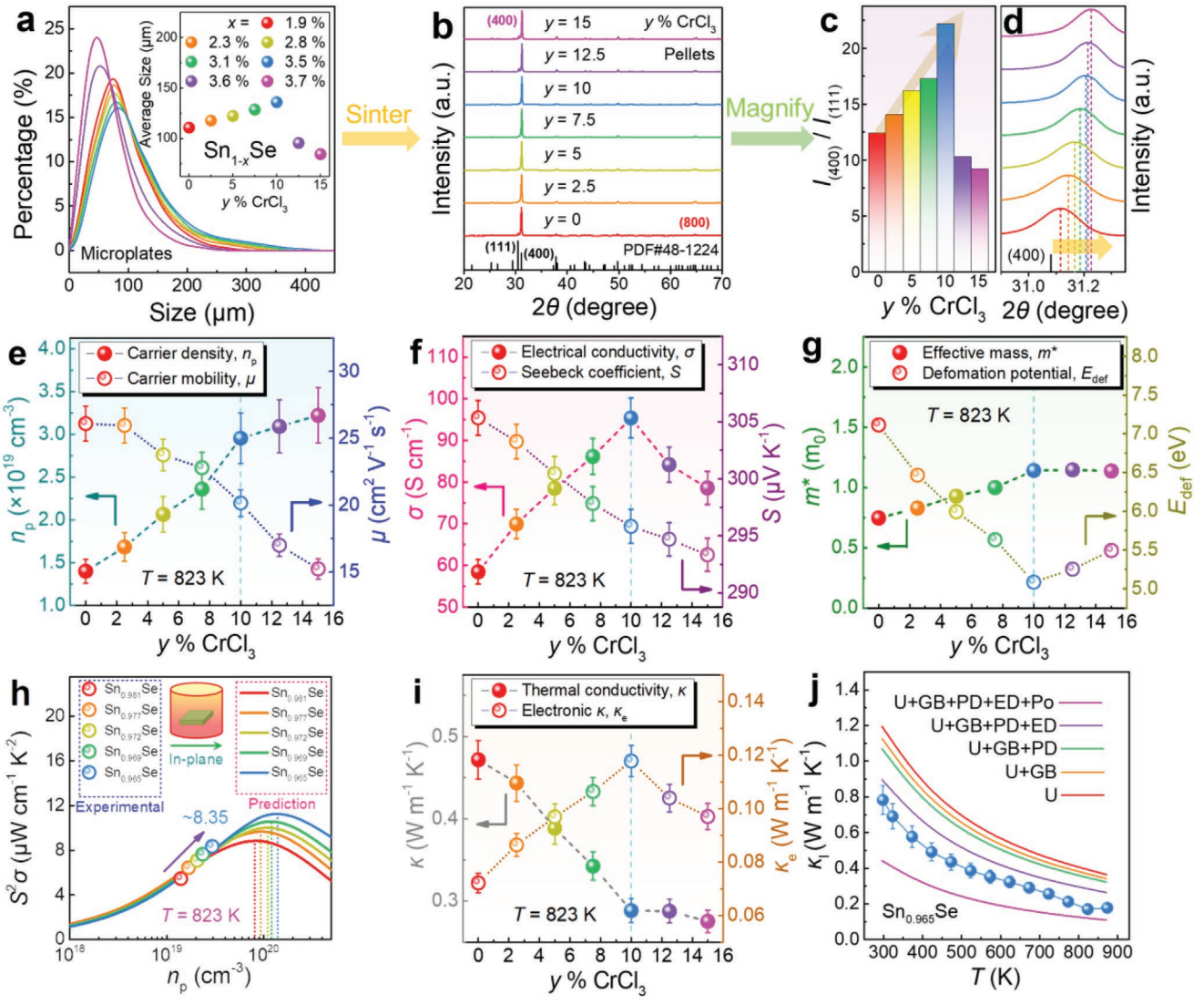

Figure 2. Anisotropy, electrical and thermal transport of polycrystalline $Sn_{1-x}Se$. a) Size distributions of solvothermally synthesized $Sn_{1-x}Se$ microplates as a function of y% $CrCl_3$. The inset shows their average sizes and compositions. b) X-ray diffraction (XRD) patterns of polycrystalline $Sn_{1-x}Se$ were fabricated by using y% $CrCl_3$ during the solvothermal synthesis. c) relative peak intensities between the (400) peak and (111) peak ($I_{(400)}/I_{(111)}$). d) Magnified XRD patterns to see the deviation of the (400) peak (right). **e**, n_p and carrier mobilities μ. f) Electrical conductivities σ and Seebeck coefficients S. g) Effective masses m^* and deformation potential coefficients E_{def}. h) n_p-dependent $S^2\sigma$ at 823 K, calculated by the SPB model. The as-achieved experimental $S^2\sigma$ values are included for comparison. i) Thermal conductivities κ and electronic thermal conductivities κ_e. j) T-dependent κ_l for polycrystalline $Sn_{0.965}Se$. Calculated κ_l by a Debye-Callaway model are included for comparison. Here U refers to the Umklapp process, GB refers to the grain boundary scattering, PD refers to the point defect scattering, ED refers to the edge dislocation scattering, and Po refers to the pore scattering.

the synthesis (Figure S10, Supporting Information). However, when the concentration of $CrCl_3$ is >10%, the dimensions of the as-synthesized microplates are significantly dropped from ≈136 μm to <100 μm because excessive $Cr(OH)_3$ in the solution will impede the crystal growth of $Sn_{1-x}Se$ microplates, while the concentration of V_{Sn} is only slightly enhanced (**Figure 2**a). After sintering these microplates into polycrystals, all samples show single-crystal-like anisotropy confirmed by their XRD patterns, in which (400) peaks exhibit the strongest intensity (Figure 2b). However, by studying the relative peak intensities between the (400) peaks and (111) peaks ($I_{(400)}/I_{(111)}$), it can be found that with increasing y from 0 to 10, $I_{(400)}/I_{(111)}$ reaches a peak value, indicating the strongest anisotropy in the as-sintered polycrystals. Oppositely, when y is >10, $I_{(400)}/I_{(111)}$ is significantly dropped, indicating the drop of anisotropy (Figure 2c). Besides, with increasing y, the (400) peaks of the as-sintered polycrystals shift toward a higher 2θ valve (Figure 2d), indicating the increased concentration of V_{Sn} as "native" point defects that shrink the lattice parameters and uni-cell volume, which is similar to the XRD results of the solvothermal synthesized microplates (Figures S11–S12, Supporting Information).

The variation of anisotropy of the as-sintered polycrystals significantly affects their electrical and thermal transport performance. In this work, we have carefully evaluated the T-dependent thermoelectric properties of polycrystalline $Sn_{1-x}Se$ as a function of y% $CrCl_3$, including measured σ, S,

and determined $S^2\sigma$ (Figure S13, Supporting Information), measured n_p and carrier mobilities μ (Figure S14), effective masses m^* and Lorenz number L calculated by the SPB model (Figure S15, Supporting Information), measured thermal diffusivities D, mass density ρ, and specific heat capacities C_p to determine the κ by $\kappa = D\rho C_p$ (Figure S16 & Table S3, Supporting Information), determined κ, κ_e, and κ_l by $\kappa_e = L\sigma T$ and $\kappa_l = \kappa - \kappa_e$ (Figure S17, Supporting Information), and determined ZT (Figure S18). All properties were evaluated along the directions both perpendicular and parallel to the sintering pressure to study their anisotropies, marked as the "⊥" and "//" directions. The results indicate that the as-achieved σ, μ, and κ are highly dependent on the anisotropy, which are much higher along the "⊥" direction (close to the in-plane direction of single crystals); while the as-achieved S and n_p are weakly dependent on the anisotropy, which are mainly determined by the compositions rather than the structures (Figures S19–S20, Supporting Information). Taking the thermoelectric properties at 823 K along the "⊥" direction for an example, with increasing the γ from 0 to 15, n_p is gradually enhanced due to the increased concentration of V_{Sn}, while μ is gradually decreased due to the strengthened scattering of carriers on the lattice imperfections in the matrix, such as point defects (mainly V_{Sn}) and grain boundaries introduced by the pores (Figure 2e). As a result, with increasing the γ from 0 to 15, S is gradually decreased due to the increased n_p, while σ is firstly increased up to a peak value of ≈95.4 S cm^{-1} at γ = 10 and then decreased, which is derived from the drop of anisotropy (Figure 2f). In terms of m^* and deformation potential coefficients E_{def} extracted from the SPB model, with increasing the γ from 0 to 15, m^* is first increased up to a peak value of ≈1.15 at γ = 10 and then kept almost stable, which is derived from the variation of n_p; while E_{def} exhibits a valley value at γ = 10, which can explain the highest texturing effect achieved in the polycrystal when γ = 10 (Figure 2g). Benefiting from the well-tuned n_p and strongest anisotropy at γ = 10, a high $S^2\sigma$ of ≈8.35 μW cm^{-1} K^{-2} can be achieved at 823 K along the "⊥" direction (Figure 2h). In terms of thermal transport, κ also exhibits a strong anisotropy-dependent feature because both κ_e and κ_l that determine the κ are related to the structures of materials. With increasing the γ from 0 to 15, κ_e is first increased up to a peak value of ≈0.12 W m^{-1} K^{-2} at γ = 10 and then decreased, which is derived from the variation of σ; while κ and κ_l are firstly decreased until γ = 10 and then kept almost unchanged, which is derived from the variation of anisotropy (Figure 2i & S17, Supporting Information). Besides, it can be found that the ratio of κ_e:κ is <40% in all samples, indicating that κ_l plays a dominant role in determining the κ. We compared the T-dependent κ_l with calculated results by a classic Debye-Callaway model (Figure 2j), in which U refers to the Umklapp process, GB refers to the grain boundary scattering, PD refers to the point defect scattering, ED refers to the edge dislocation scattering, and Po refers to the pore scattering. The pores play a significant role in determining the low κ_l. Furthermore, our achieved thermoelectric properties possess high repeatability/stability, confirmed by the repetition tests (Figure S21, Supporting Information).

To understand the as-achieved low κ_l, we investigate comprehensive microstructure characterizations on the solvothermal synthesized microplates and as-sintered polycrystals. Taking $Sn_{0.965}Se$ for a typical case (γ = 10), benefited from the $Cr(OH)_3$ colloidal precipitations that act as "templates" during the solvothermal synthesis, the as-synthesized $Sn_{0.965}Se$ microplates are highly porous but successfully keep a large average size (**Figure 3**a), especially compared to the dense $Sn_{0.981}Se$ microplates when no $CrCl_3$ was used (Figure S22, Supporting Information). After sintering these porous microplates into bulk materials, although most of the pores in the microplates were compressed by the high sintering pressure, the as-achieved polycrystal still successfully keeps some micro/nanopores as 3D crystal imperfections (Figure 3b). The average diameter of pores in $Sn_{0.965}Se$ is ≈1.2 μm (Figure S8, Supporting Information). It was pointed out that the thermal transport in pores is only based on thermal radiation,[19] and the boundaries of the pores can strongly scatter the phonons with different wavelengths,[19] therefore micro/nanopores are useful to suppress the κ. Similar to the polycrystalline $Sn_{0.981}Se$ (Figure S23, Supporting Information), the strong anisotropy of polycrystalline $Sn_{0.965}Se$ is also safely kept, derived from the large average size of the $Sn_{0.965}Se$ microplates. The anisotropy of polycrystalline $Sn_{0.965}Se$ is even stronger than that of polycrystalline $Sn_{0.981}Se$, confirmed by their XRD results (Figure S24, Supporting Information). Besides, the distributions of Sn and Se elements are uniform after sintering confirmed by energy-dispersive spectroscopy (EDS) results, indicating that there is no composition change during the sintering process (Figure S25, Supporting Information).

To further study the structure characteristics, we investigated scanning tunneling microscopy (STM), transmission electron microscopy (TEM), and spherical aberration-corrected scanning TEM (Cs-STEM) characterizations. In detail, we used STM to characterize the surface of polycrystalline $Sn_{0.965}Se$, and the results show a typical surface with dense V_{Sn} as point defects (Figure 3c). These V_{Sn} are individually distributed, and no extra atomic plane is extended from the V_{Sn}, indicating that these defects are Sn vacancies rather than parts of dislocations. Around these V_{Sn}, the lattices are distorted, resulting in different contrast from the matrix without V_{Sn}. Such a contrast around the V_{Sn} is derived from the release of hole carriers by the V_{Sn}, which causes the change of charge distribution around the V_{Sn} detected by the tunnel current of STM. The inset image shows a corresponding magnified STM image after a fast Fourier transform (FFT) taken from a normal area, in which the Sn and Se atoms are both labeled on this (100) surface (b–c plane). In addition to STM, TEM and Cs-STEM were also employed to study the lattice features of $Sn_{1-x}Se$ microplates (Figures S26–S27, Supporting Information) and polycrystals. For example, the high-resolution TEM (HRTEM) result of polycrystalline $Sn_{0.965}Se$ shows typical lattice distortions (Figure 3d), which are mainly caused by the V_{Sn}. These lattice distortions cause significant lattice strains in the matrix (Figure S28, Supporting Information), which act as the effective sources for short-wavelength phonon scattering. As well, the V_{Sn} can be observed by Cs-STEM high-angle annular dark-field (HAADF) image (Figure 3e). In addition to the V_{Sn} as typical point defects, grain boundaries are also typical lattice imperfections in polycrystalline $Sn_{0.965}Se$. For example, one typical grain boundary is observed by the HRTEM image (Figure 3f), in which the adjacent grains possess close zone axes, confirmed

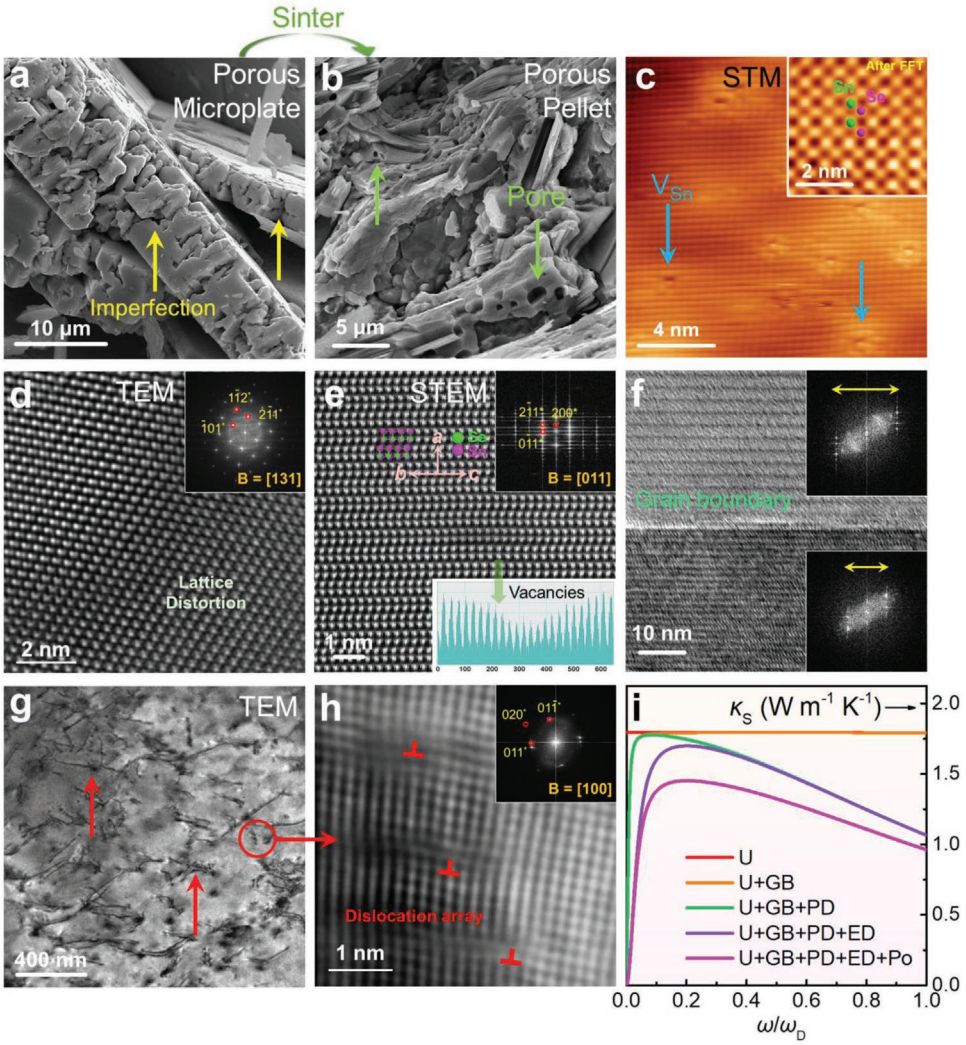

Figure 3. Micro/nanostructural characterizations of polycrystalline $Sn_{1-x}Se$. a) Scanning electron microscopy (SEM) image of solvothermally synthesized $Sn_{0.965}Se$ microplates by using 10% $CrCl_3$. b) SEM image of cracked polycrystalline $Sn_{0.965}Se$ to show the pores. **c**, Scanning tunneling microscopy (STM) image of the surface of polycrystalline $Sn_{0.965}Se$ to show the Sn vacancies (V_{Sn}). The inset shows a corresponding magnified STM image after a fast Fourier transform (FFT) taken from a normal area. d) High-resolution transmission electron microscopy (HRTEM) image of polycrystalline $Sn_{0.965}Se$ to show the lattice distortion. The TEM sample is prepared by the focused ion beam (FIB) technique. The inset shows the corresponding FFT pattern. e) Spherical aberration-corrected scanning transmission electron microscopy (Cs-STEM) high-angle annular dark-field (HAADF) image of polycrystalline $Sn_{0.965}Se$ to show the local V_{Sn} domain. The insets show the corresponding FFT pattern (top-right) and line profile (bottom-right) taken from the local V_{Sn} domain. f) HRTEM image of polycrystalline $Sn_{0.965}Se$ to show the grain boundary. The insets compare the FFT patterns of the adjacent grains. g) TEM image of polycrystalline $Sn_{0.965}Se$ to show dense edge dislocations. h) Corresponding HRTEM image to show an array of dislocations with typical edge characteristics. i) Calculated spectral lattice thermal conductivity (κ_s) at 300 K using the Debye-Callaway model.

by their FFT patterns. Benefiting from the micro/nanoporous structure of solvothermally synthesized $Sn_{0.965}Se$ microplates, the as-sintered polycrystals possess considerably dense grain boundaries (Figure S29, Supporting Information), derived from the nanograins formed by squeezing the micro/nanoporous structure of microplates through high-pressure SPS. The dense grain boundaries are effective sources for long-wavelength phonon scattering. Besides, in the matrix of polycrystalline $Sn_{0.965}Se$, we also found dense dislocations confirmed by the TEM image (Figure 3g). After magnifying one of these dislocations, an array of dislocations can be observed that show typical edge characteristics, confirmed by the corresponding HRTEM image (Figure 3h). These dislocations are mainly triggered by V_{Sn} when the lattice distortions caused by the V_{Sn} are strong enough to meet the dislocation formation energy. Similar to V_{Sn}, dislocations especially edge dislocations can also cause significant lattice strains (Figure S30, Supporting Information),[4] which are effective sources for mid-wavelength phonon scattering. It should be noted that most dislocations found in thermoelectric materials are curved, indicating that they have a mixed nature, and only the edge component of dislocation can be seen in HRTEM images.[4] The edge dislocations are also effective for improving the mechanical properties of thermoelectric materials. Based on the as-observed multi-dimensional lattice imperfections, we used the Debye-Callaway model to calculate the spectral lattice thermal conductivity (κ_s)

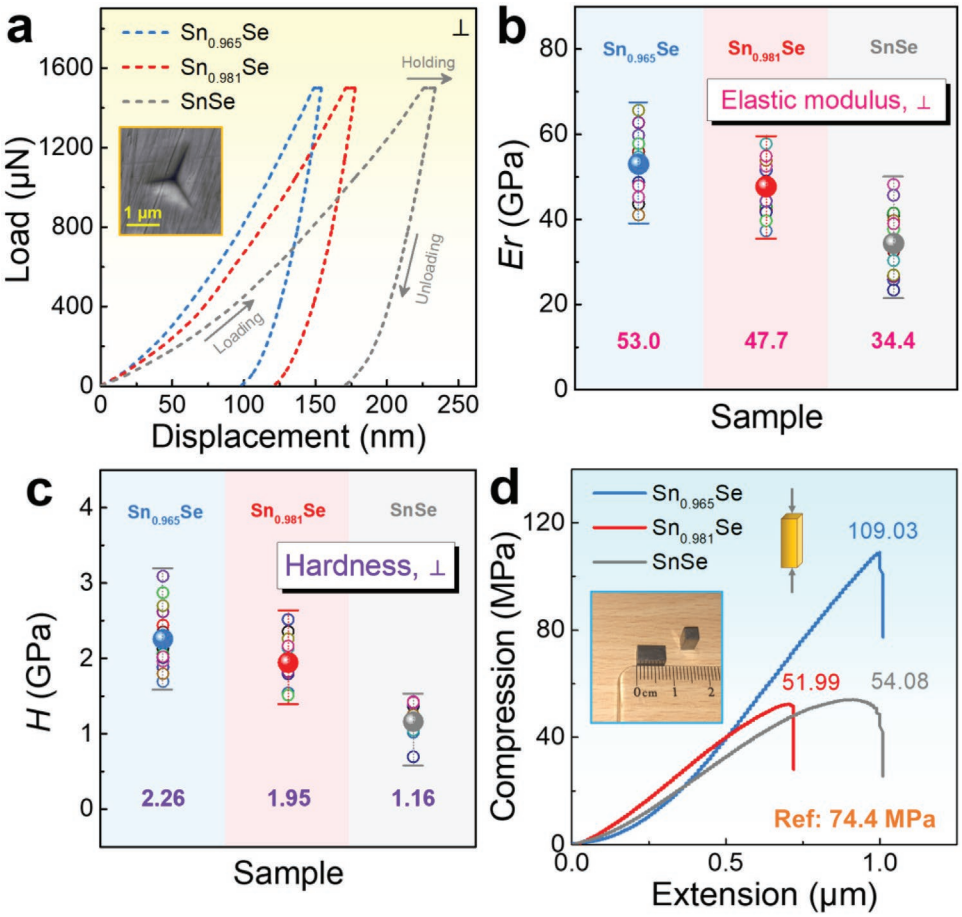

Figure 4. Mechanical Performance of polycrystalline $Sn_{1-x}Se$. a) Load-displacement curves. The inset SEM image shows typical nanoindentation. b) Elastic modules *Er*. c) hardness *H*. d) Compressive strength with reported value.[37] The inset photo shows typical specimens used for the compression tests.

of polycrystalline $Sn_{0.965}Se$ at 300 K (Figure 3i). Benefiting from the point defects, edge dislocations, dense grain boundaries, and micro/nanopores, it is reasonable to achieve the low κ_l in the as-fabricated polycrystals. It should be noted that a few $Cr(OH)_3$ precipitations may be occasionally included in the matrix of polycrystals due to the insufficient cleaning of solvothermally synthesized microplates, which can act as "nanoinclusions" to scatter the phonons (Figure S31, Supporting Information). However, considering that these nanoinclusions are still impurities that may harm electrical and mechanical performance, these impurities should be removed.

In addition to optimizing the thermoelectric performance of polycrystalline $Sn_{1-x}Se$, $CrCl_3$ can simultaneously improve its mechanical properties, which are crucial for employing in practical devices for long-term durability. Here, we further evaluated the local elastic modules *Er* and hardness *H* by a nanoindenter, and the overall compressive strength by a conventional compression test. The samples include polycrystalline $Sn_{0.965}Se$ ($\gamma = 10$), polycrystalline $Sn_{0.981}Se$ ($\gamma = 0$), and SnSe with rare V_{Sn} and poor anisotropy, fabricated by a conventional melting route. The nanoindentation tests were under fixed loads of 1500 μN on the polycrystal surfaces perpendicular to the sintering pressure (⊥ direction), which is the same as the direction of the as-achieved thermoelectric performance. As well, considering that the nanoindentation may be taken on the grain boundaries or scratches caused by the polishing paper, to ensure convincing results, each sample was measured 15 times. Polycrystalline $Sn_{0.965}Se$ exhibits the lowest displacement among the three samples during the nanoindentation tests (**Figure 4**a), indicating potentially high local *Er* and *H*. The inset shows a SEM image of typical nanoindentation. The size of the nanoindentation is only ≈1 μm, and the depth is within 300 nm. After further analyzing the load-displacement curves, we found that polycrystalline $Sn_{0.965}Se$ exhibits the highest *Er* and *H* (Figures 4b,c). Compared with the reported *H* value of ≈0.27 GPa in SnSe,[31] the average *H* of ≈2.26 GPa achieved in our polycrystalline $Sn_{0.965}Se$ is much higher. Meanwhile, this value is also highly competitive compared to other commercial thermoelectric materials such as Bi_2Te_3.[32] Such high *Er* and *H* values are mainly derived from the as-observed V_{Sn}-induced lattice distortions and dislocations, which are effective in improving the local mechanical properties. Sn vacancies that act as intrinsic point defects can cause significant lattice distortions, which impede the dislocation movement and make the dislocation difficult to slip, thereby increasing the strength and hardness of the material. Such a strengthening mechanism is similar to some reported

alloys.[33] As well, the strengthening in *Er* and *H* is also partially derived from the V_{Sn}-induced dispersion strengthening for the grains.[34–36] Besides, we found that the *Er* and *H* values measured along the ⊥ direction are higher than the//direction for all samples, which are mainly derived from the anisotropy difference (Figure S32, Supporting Information). It should be also noted that the nanoindentation results mostly reflect the mechanical properties of a targeted small area, and this is why we further undertook the compression test, which can reflect the entire mechanical properties of the polycrystals.

Considering that the materials in thermoelectric modules may experience significant stress (mainly compression) during in-service, the materials need to have high compressive strengths. In terms of the compression tests, all samples were cut into cuboidal chips of 3.5 mm in width and thickness, and 7 mm in length (Figure S33, Supporting Information). The direction for compression is also along the ⊥ direction. The strain rate was set as 2.5×10^{-4} s^{-1} for all samples. From the compression-extension curves (Figure 4d), the compressive strength of $Sn_{0.965}Se$ (109.03 MPa) is much higher than $Sn_{0.981}Se$ (51.99 MPa) and SnSe (54.08 MPa), as well as reported value (74.4 MPa),[37] indicating that $Sn_{0.965}Se$ possesses excellent mechanical properties at a macroscale. Such high performance is mainly derived from the dense grain boundaries of the polycrystals sintered from the micro/nanoporous structure of microplates. During the sintering process, most of the pores in the microplates were compressed by the high pressure, leading to an effect of grain refinement, which can further strengthen the mechanical properties of pellets according to the Hall-Petch relationship $\delta = \delta_0 + Kg^{-1/2}$, where δ and δ_0 are yield strengths of polycrystal and single crystal, respectively, K is a constant, and g is the average grain size.[38,39] By reducing the g, the yield strength is enhanced, fitting well with our experimental results. Meanwhile, it should be noted that the extension of $Sn_{0.981}Se$ is much lower than $Sn_{0.965}Se$ and SnSe, this is because $Sn_{0.981}Se$ possesses stronger anisotropy but fewer grain boundaries than SnSe. As a result, during the compression test, the pressure prefers to break the Van der Waals forces between Sn-Se layers of $Sn_{0.981}Se$ polycrystal and in turn, leads to a crack along the in-plane direction. Our compression results also exhibit anisotropy (Figure S34, Supporting Information).

To evaluate the potential of polycrystalline $Sn_{0.965}Se$ for applying to practical thermoelectric devices, we evaluate its theoretical maximum energy conversion efficiency η_{max} based on the calculated ZT_{ave} (**Figure 5**a). In this work, the ZT_{ave} is calculated in two different ways, namely conventional

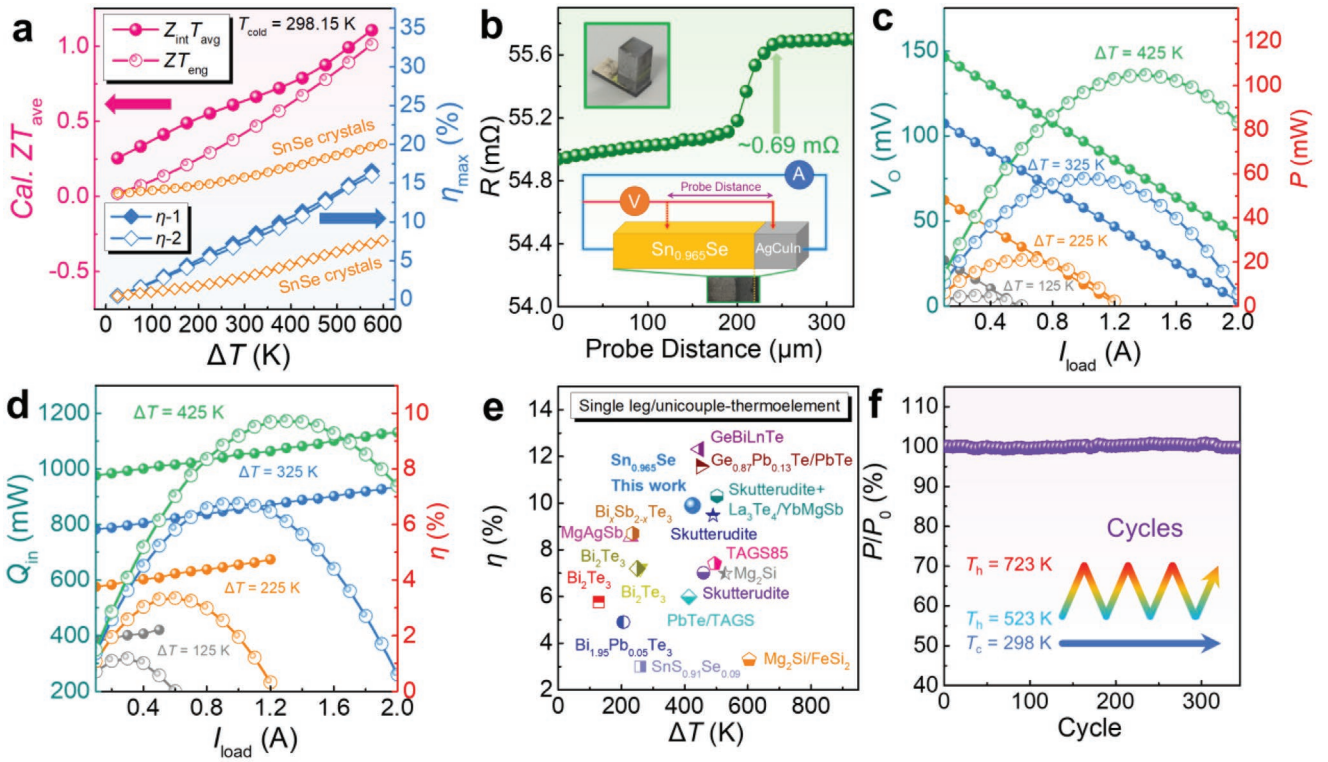

Figure 5. Single-leg thermoelectric device based on polycrystalline $Sn_{0.965}Se$ and its power generation performance. a) Calculated average ZT (ZT_{ave}) and corresponding maximum energy conversion efficiency η_{max} of polycrystalline $Sn_{0.965}Se$. The ZT_{ave} are calculated in two different ways, namely conventional average figure-of-merit ($Z_{int}T_{ave}$) calculated by integration, and the engineering figure-of-merit (ZT_{eng}) that accounts for the cumulative temperature-dependent thermoelectric properties.[14] Here η-1 correspondes to $Z_{int}T_{ave}$, and η-2 correspondes to ZT_{eng}. The corresponding results taken from the reported p-type SnSe crystals are included for comparison.[10] b) Resistivity (R) across the interface between $Sn_{0.965}Se$ and AgCuIn solder. The insets show the photo of the single-leg device (top-left) and the illustration of the measurement (bottom). c) output voltage (V_o) and power (P) as a function of loading current (I_{load}) under different temperature differences (ΔT). d) Input heat flow (Q_{in}) from the hot side, and conversion efficiency (η) as a function of I_{load} under different ΔT. e) Comparison of η between our single-leg device and reported values.[40–54] f) Relative output power (P/P_0) of the single-leg device as a function of thermal cycling time.

average figure-of-merit ($Z_{int}T_{ave}$) calculated by integration, and engineering figure-of-merit (ZT_{eng}) that accounts for the cumulative T-dependent thermoelectric properties.[14] Therefore, ZT_{eng} is more useful for exactly determining the η_{max} for a given material at a large temperature difference (ΔT) between the cold and hot sides, and the dimensionless intensity factor of the Thomson coefficient $\hat{\alpha}$ needs to be considered during calculating the η_{max} based on ZT_{eng} (Figure S35, Supporting Information). Here η-1 and η-2 are calculated based on $Z_{int}T_{ave}$ and ZT_{eng}, respectively, and the corresponding results taken from the reported p-type SnSe crystals are included for comparison.[10] Clearly, the ZT_{eng} of our polycrystalline $Sn_{0.965}Se$ is much higher than that of reported p-type SnSe crystals, which can contribute to a η_{max} of ≈17% at a ΔT of 575 K. Considering that the practical η_{max} should also be evaluated due to the resistivity (R) between the thermoelectric materials and solder, we fabricated a single-leg thermoelectric device composed of polycrystalline $Sn_{0.965}Se$ as thermoelectric leg and AgCuIn solder as a binder to connect the leg and Cu-Al_2O_3 substrate (Figure S36, Supporting Information). The R across the interface between $Sn_{0.965}Se$ and AgCuIn solder is ≈0.69 mΩ, which can be neglected since the R of $Sn_{0.965}Se$ is >50 mΩ at room temperature (Figure 5b). We measured the output voltage (V_o) and power (P) of the as-fabricated single-leg device as a function of loading current (I_{load}) under different ΔTs, performed in a vacuum environment. The results indicate that a ΔT of 425 K can lead to a peak P of >100 mW when I_{load} = 1.4 A (Figure 5c). Considering the dimensions of the single leg are 3.95 mm in width and thickness and 6 mm in length, the determined power density is ≈1175 mW cm^{-3}. Besides, we measured the input heat flow (Q_{in}) from the hot side and obtained conversion efficiency (η) as a function of I_{load} under different ΔT (Figure 5d). The evaluated maximum practical η is ≈10%, which is competitive compared to other single-leg thermoelectric devices (Figure 5e).[40–54] It should be noted that a single-leg device always tends to overestimate its efficiency. In addition to the high power generation performance, the as-fabricated device possesses high stability, confirmed by its stable relative output power (P/P_0) of ≈100% as a function of thermal cycling time up to 350 (Figure 5f). The temperature for the cold side (T_c) is fixed as 298 K, while the temperature for the hot side (T_h) is cycled between 723 K and 523 K. All these results confirm the promising practical value of polycrystalline $Sn_{0.965}Se$ for applying to thermoelectric devices. Because SnSe is highly sensitive to oxygen, the oxidization of SnSe can severely damage its electrical and thermal transport, therefore SnSe-based thermoelectric devices must be carefully protected and better be employed in a vacuum environment. Meanwhile, to further improve the η of SnSe-based thermoelectric devices, exploring high-performance n-type SnSe-based thermoelectric materials is also of significance. More studies are needed to further improve the η by rational device design, such as structure, topology, electrode, and insulating filler.[4]

3. Conclusion

In this work, by simply tuning the amount of $CrCl_3$ during the solvothermal synthesis, highly micro/nanoporous $Sn_{1-x}Se$ microplates with large dimensions and well-tuned n_p can be successfully achieved. After sintering these microplates into polycrystals, the as-achieved bulk materials exhibit structures with strong anisotropy and multi-dimensional crystal/lattice imperfections. The optimized n_p of ≈3×10^{19} cm^{-3} comes from the enhanced V_{Sn} concentration triggered by the common ion effect of Cl^- provided by $CrCl_3$, leading to a high $S^2\sigma$ of ≈8.35 μW cm^{-1} K^{-2} at 823 K; while the formed $Cr(OH)_3$ colloidal precipitations act as unique "templates" to form micro/nanopores in the microplates during synthesis. These micro/nanopores combined with V_{Sn} as point defects, intensive edge dislocations triggered by V_{Sn}, and dense grain boundaries contribute to a low κ_l of ≈0.2 W m^{-1} K^{-1} at 823 K, which lead to a high peak ZT of ≈2.4 at this temperature and a high ZT_{ave} of ≈1.1. The as-achieved polycrystals simultaneously exhibit good mechanical properties with a high H of ≈2.26 GPa and a compression strength of ≈109 MPa, while the as-fabricated single-leg device shows stable P of >100 mW and η of ≈10% at a ΔT of 425 K, indicating great potential for applying to practical thermoelectric devices. This work provides a unique route to realize high thermoelectric and mechanical performance in polycrystalline materials from an aspect of solvothermal synthetic environmental design.

4. Experimental Section

Experimental Details are provided in the Supporting Information.

Supporting Information

Supporting Information is available from the Wiley Online Library or from the author.

Acknowledgements

This work was financially supported by the Australian Research Council. The Australian Microscopy & Microanalysis Research Facility was acknowledged for providing characterization facilities. Research Computing Centre at the University of Queensland and the National Computational Infrastructure supported by the Australian Government were acknowledged for providing computing facilities. The authors acknowledge A.Y.W., W.Y.C., T.Y.C., B.X.H., and V.T.N. for discussion and sample preparation. The authors acknowledge H.F.F. and Y.D. for the help in STM characterizations.

Open access publishing facilitated by Queensland University of Technology, as part of the Wiley - Queensland University of Technology agreement via the Council of Australian University Librarians.

Conflict of Interest

The authors declare no conflict of interest.

Data Availability Statement

The data that support the findings of this study are available from the corresponding author upon reasonable request.

Keywords

devices, SnSe, solvothermal, thermoelectric, vacancies

Received: February 25, 2022
Revised: March 19, 2022
Published online: April 11, 2022

[1] G. J. Snyder, E. S. Toberer, *Nat. Mater.* **2008**, *7*, 105.
[2] Y. Zheng, T. J. Slade, L. Hu, X. Y. Tan, Y. Luo, Z.-Z. Luo, J. Xu, Q. Yan, M. G. Kanatzidis, *Chem. Soc. Rev.* **2021**, *50*, 9022.
[3] X. Shi, L. Chen, *Nat. Mater.* **2016**, *15*, 691.
[4] X.-L. Shi, J. Zou, Z.-G. Chen, *Chem. Rev.* **2020**, *120*, 7399.
[5] Y. Xiao, L.-D. Zhao, *Science* **2020**, *367*, 1196.
[6] X. Zhang, Z. Bu, S. Lin, Z. Chen, W. Li, Y. Pei, *Joule* **2020**, *4*, 986.
[7] W. Liu, L. Yang, Z.-G. Chen, J. Zou, *Adv. Mater.* **2020**, *32*, 1905703.
[8] Y. Pei, X. Shi, A. LaLonde, H. Wang, L. Chen, G. J. Snyder, *Nature* **2011**, *473*, 66.
[9] L.-D. Zhao, C. Chang, G. Tan, M. G. Kanatzidis, *Energy Environ. Sci.* **2016**, *9*, 3044.
[10] L. D. Zhao, S. H. Lo, Y. Zhang, H. Sun, G. Tan, C. Uher, C. Wolverton, V. P. Dravid, M. G. Kanatzidis, *Nature* **2014**, *508*, 373.
[11] C. Chang, M. Wu, D. He, Y. Pei, C.-F. Wu, X. Wu, H. Yu, F. Zhu, K. Wang, Y. Chen, *Science* **2018**, *360*, 778.
[12] S. H. Heo, S. Jo, H. S. Kim, G. Choi, J. Y. Song, J.-Y. Kang, N.-J. Park, H. W. Ban, F. Kim, H. Jeong, *Nat. Commun.* **2019**, *10*, 864.
[13] C. Zhou, Y. K. Lee, Y. Yu, S. Byun, Z.-Z. Luo, H. Lee, B. Ge, Y.-L. Lee, X. Chen, J. Y. Lee, O. Cojocaru-Mirédin, H. Chang, J. Im, S.-P. Cho, M. Wuttig, V. P. Dravid, M. G. Kanatzidis, I. Chung, *Nat. Mater.* **2021**, *20*, 1378.
[14] H. S. Kim, W. Liu, G. Chen, C.-W. Chu, Z. Ren, *Proc. Natl. Acad. Sci. U. S. A.* **2015**, *112*, 8205.
[15] X.-L. Shi, W.-D. Liu, A.-Y. Wu, V. T. Nguyen, H. Gao, Q. Sun, R. Moshwan, J. Zou, Z.-G. Chen, *InfoMat* **2020**, *2*, 1201.
[16] X. Shi, A. Wu, T. Feng, K. Zheng, W. Liu, Q. Sun, M. Hong, S. T. Pantelides, Z. G. Chen, J. Zou, *Adv. Energy Mater.* **2019**, *9*, 1803242.
[17] M. Jin, X.-L. Shi, T. Feng, W. Liu, H. Feng, S. T. Pantelides, J. Jiang, Y. Chen, Y. Du, J. Zou, Z.-G. Chen, *ACS Appl. Mater. Interfaces* **2019**, *11*, 8051.
[18] W. Wei, C. Chang, T. Yang, J. Liu, H. Tang, J. Zhang, Y. Li, F. Xu, Z. Zhang, J.-F. Li, G. Tang, *J. Am. Chem. Soc.* **2018**, *140*, 499.
[19] X. Shi, A. Wu, W. Liu, R. Moshwan, Y. Wang, Z.-G. Chen, J. Zou, *ACS Nano* **2018**, *12*, 11417.
[20] M. Dargusch, X.-L. Shi, X. Q. Tran, T. Feng, F. Somidin, X. Tan, W. Liu, K. Jack, J. Venezuela, H. Maeno, T. Toriyama, S. Matsumura, S. T. Pantelides, Z.-G. Chen, *J. Phys. Chem. Lett.* **2019**, *10*, 6512.
[21] C. Liu, L. Miao, X. Wang, S. Wu, Y. Zheng, Z. Deng, Y. Chen, G. Wang, X. Zhou, *Chin. Phys. B* **2018**, *27*, 047211.
[22] G. Tang, Q. Wen, T. Yang, Y. Cao, W. Wei, Z. Wang, Z. Zhang, Y. Li, *RSC Adv.* **2017**, *7*, 8258.
[23] Y. Li, F. Li, J. Dong, Z. Ge, F. Kang, J. He, H. Du, B. Li, J.-F. Li, *J. Mater. Chem. C* **2016**, *4*, 2047.
[24] Z.-H. Ge, K. Wei, H. Lewis, J. Martin, G. S. Nolas, *J. Solid State Chem.* **2015**, *225*, 354.
[25] C. Wang, Y. Li, G. Zhang, J. Zhuang, G. Shen, *Inorg. Chem.* **2000**, *39*, 4237.
[26] L. F. Amaral, I. R. Oliveira, R. Salomão, E. Frollini, V. C. Pandolfelli, *Ceram. Int.* **2010**, *36*, 1047.
[27] M. R. Burton, S. Mehraban, D. Beynon, J. McGettrick, T. Watson, N. P. Lavery, M. J. Carnie, *Adv. Energy Mater.* **2019**, *9*, 1900201.
[28] S. R. Popuri, M. Pollet, R. Decourt, F. D. Morrison, N. S. Bennett, J. W. G. Bos, *J. Mater. Chem. C* **2016**, *4*, 1685.
[29] Y. Fu, J. Xu, G.-Q. Liu, J. Yang, X. Tan, Z. Liu, H. Qin, H. Shao, H. Jiang, B. Liang, J. Jiang, *J. Mater. Chem. C* **2016**, *4*, 1201.
[30] M. Jin, Z. Tang, R. Zhang, L. Zhou, X. Wang, R. Li, *J. Alloys Compd.* **2020**, *824*, 153869.
[31] K. Tyagi, B. Gahtori, S. Bathula, N. K. Singh, S. Bishnoi, S. Auluck, A. K. Srivastava, A. Dhar, *RSC Adv.* **2016**, *6*, 11562.
[32] L.-D. Zhao, B.-P. Zhang, J.-F. Li, M. Zhou, W.-S. Liu, J. Liu, *J. Alloys Compd.* **2008**, *455*, 259.
[33] P. Thirathipviwat, G. Song, J. Bednarcik, U. Kühn, T. Gemming, K. Nielsch, J. Han, *Prog. Nat. Sci.* **2020**, *30*, 545.
[34] G. Hasemann, J. Schneibel, M. Krüger, E. P. George, *Intermetallics* **2014**, *54*, 95.
[35] Y. N. Osetsky, D. J. Bacon, *Mater. Sci. Eng. A* **2005**, *400*, 374.
[36] Y.-J. Li, Q.-M. Hu, D.-S. Xu, R. Yang, *Intermetallics* **2011**, *19*, 793.
[37] J. Fu, X. Su, H. Xie, Y. Yan, W. Liu, Y. You, X. Cheng, C. Uher, X. Tang, *Nano Energy* **2018**, *44*, 53.
[38] E. O. Hall, *Proc. Phys. Soc., Sect. B* **1951**, *64*, 747.
[39] N. J. Petch, *Iron Steel Inst.* **1953**, *174*, 25.
[40] W. Liu, Q. Jie, H. S. Kim, Z. Ren, *Acta Mater.* **2015**, *87*, 357.
[41] S. Perumal, M. Samanta, T. Ghosh, U. S. Shenoy, A. K. Bohra, S. Bhattacharya, A. Singh, U. V. Waghmare, K. Biswas, *Joule* **2019**, *3*, 2565.
[42] W. He, D. Wang, H. Wu, Y. Xiao, Y. Zhang, D. He, Y. Feng, Y.-J. Hao, J.-F. Dong, R. Chetty, *Science* **2019**, *365*, 1418.
[43] A. K. Bohra, R. Bhatt, A. Singh, S. Bhattacharya, R. Basu, K. N. Meshram, S. K. Sarkar, P. Bhatt, P. K. Patro, D. K. Aswal, K. P. Muthe, S. C. Gadkari, *Mater. Des.* **2018**, *159*, 127.
[44] L. I. Anatychuk, L. N. Vikhor, L. T. Strutynska, I. S. Termena, *J. Electron. Mater.* **2011**, *40*, 957.
[45] D. Kraemer, J. Sui, K. McEnaney, H. Zhao, Q. Jie, Z. F. Ren, G. Chen, *Energy Environ. Sci.* **2015**, *8*, 1299.
[46] A. Singh, S. Bhattacharya, C. Thinaharan, D. K. Aswal, S. K. Gupta, J. V. Yakhmi, K. Bhanumurthy, *J. Phys. D: Appl. Phys.* **2008**, *42*, 015502.
[47] J. R. Salvador, J. Y. Cho, Z. Ye, J. E. Moczygemba, A. J. Thompson, J. W. Sharp, J. D. Koenig, R. Maloney, T. Thompson, J. Sakamoto, *Phys. Chem. Chem. Phys.* **2014**, *16*, 12510.
[48] I. Aoyama, H. Kaibe, L. Rauscher, T. Kanda, M. Mukoujima, S. Sano, T. Tsuji, *Jpn. J. Appl. Phys.* **2005**, *44*, 4275.
[49] E. Groβ, M. Riffel, U. Stöhrer, *J. Mater. Res.* **1995**, *10*, 34.
[50] T. Caillat, J. Fleurial, G. J. Snyder, A. Borshchevsky, in *Proc. ICT2001. 20 Int. Conf. Thermoelectrics (Cat. No.01TH8589)*, Beijing, China June **2001**, pp. 8–11.
[51] A. Muto, J. Yang, B. Poudel, Z. Ren, G. Chen, *Adv. Energy Mater.* **2013**, *3*, 245.
[52] Y. Gelbstein, J. Davidow, S. N. Girard, D. Y. Chung, M. Kanatzidis, *Adv. Energy Mater.* **2013**, *3*, 815.
[53] S. E. Yang, F. Kim, F. Ejaz, G. S. Lee, H. Ju, S. Choo, J. Lee, G. Kim, S.-h. Jung, S. Ahn, H. G. Chae, K. T. Kim, B. Kwon, J. S. Son, *Nano Energy* **2021**, *81*, 105638.
[54] T. Kuroki, K. Kabeya, K. Makino, T. Kajihara, H. Kaibe, H. Hachiuma, H. Matsuno, A. Fujibayashi, *J. Electron. Mater.* **2014**, *43*, 2405.